Article:
Skelton, R and Walker, AM orcid.org/0000-0003-3121-3255 (2018) Lubrication of dislocation glide in MgO by hydrous defects. Physics and Chemistry of Minerals, 45 (8). pp. 713-726. ISSN 0342-1791

https://doi.org/10.1007/s00269-018-0957-y

Lubrication of dislocation glide in MgO by hydrous defects

Richard Skelton [a,*] and Andrew M. Walker[b]

[a] Research School of Earth Sciences, Australian National University, Canberra, ACT, 0200, Australia

(ORCID: 0000-0003-1583-2312)

[b] School of Earth and Environment, University of Leeds, Leeds, LS2 9JT, UK

(ORCID: 0000-0003-3121-3255)

* Corresponding author: richard.skelton@anu.edu.au

Abstract

Water-related defects, principally in the form of protonated cation vacancies, are potentially able to weaken minerals under high-stress or low-temperature conditions by reducing the Peierls stress required to initiate dislocation glide. In this study, we use the Peierls-Nabarro (PN) model to determine the effect of protonated Mg vacancies on the 1/2<110>{110} and 1/2<110>{100} slip systems in MgO. This PN model is parameterized using generalized stacking fault energies calculated using plane-wave density functional theory, with and without protonated Mg vacancies present at the glide plane. It found that these defects increase dislocation core widths and reduce the Peierls stress over the entire pressure range 0-125 GPa. Furthermore, 1/2<110>{110} slip is found to be more sensitive to the presence of protonated vacancies which increases in the pressure at which {100} becomes the easy glide plane for 1/2<110> screw dislocations. These results demonstrate, for a simple mineral system, that water-related defects can alter the deformation

behavior of minerals in the glide-creep regime by reducing the stress required to move dislocations by glide. (Mg, Fe)O is the most anisotropic mineral in the Earth's lower mantle, so the differential sensitivity of the major slip systems in MgO to hydrous defects has potential implications for the interpretation of the seismic anisotropy in this region.

Keywords

MgO; dislocations; hydrous defects; Peierls stress; Peierls-Nabarro modeling

1. Introduction

Dislocations are linear topological defects in a crystal lattice that act as carriers of plastic strain. The stress required to move a dislocation by glide is lower than the ideal shear strength of a crystal, and glide-controlled creep can be a significant contributor to deformation, especially under conditions of moderate to high stress or low temperature. Dislocations can also act as reservoirs for point defects, as the strain fields around the core induce elastic and inelastic interactions between point defects and dislocations that cause segregation of point defects to dislocation cores. This can diminish dislocation mobility through the phenomenon of solute drag, whereby the additional energy required to either pull a solute cloud along with a translating dislocation or break free from it altogether increases the stress required for dislocation creep (Cottrell and Bilby 1949). Alternatively, in the glide-creep regime, point defects can enhance dislocation mobility, by reducing the stress required to initiate glide at 0 K (the Peierls stress, σ_p).

Vacancies have been found to reduce stacking fault energies and lubricate dislocation glide in a variety of metals, including fcc Al (Lauzier et al. 1989; Lu and Kaxiras 2002), Ni, Cu, Fe (Asadi et al. 2014). Vacancies can also reduce the Peierls stress in non-metals, such as the superconductor MgB_2 (Shen et al. 2015). Theoretical calculations show that hydrogen can lubricate dislocation

glide in fcc metals such Al (Lu et al. 2001) and Fe (Taketomi et al. 2008), which may explain the ubiquitous phenomenon of hydrogen induced local plasticity in these metals. Chemical impurities, in the form of interstitial oxygen defects, can also lubricate dislocation glide in oxides such as UO_2, decreasing the critical resolved shear stress and changing the relative strength of its major slip systems (Keller et al. 1988). This is attributed to interactions between dislocation cores and the interstitial oxygen ions reducing the Peierls barrier to glide (Ashbee and Yust 1982).

(Mg, Fe)O is thought to be the second most abundant mineral in the Earth's lower mantle, after the perovskite-structured mineral (Mg, Fe)SiO_3 bridgmanite, comprising slightly less than 20% of the region's volume (eg. Lee et al. 2004). Despite being less abundant than bridgmanite, the relatively low strength of (Mg, Fe)O means that it may accommodate the majority of the strain in lower-mantle rocks (Girard et al. 2016). Along a mantle geotherm, MgO deforms athermally to ~2000km depth, with dislocation-dislocation interactions governing flow rates. At greater depths, the rheology is in the thermally activated regime and the Peierls stress becomes important for determining strain rates (Cordier et al. 2012). In MgO, the dominant slip system at ambient pressure is 1/2<110>{110}, with a modest additional contribution from the 1/2<110>{100} slip system. High pressure creep experiments show that the relative activity of the 1/2<110>{100} slip system in MgO gradually increases with pressure and, above ~23 GPa, this slip system comes to dominate over the 1/2<110>{110} slip system (Girard et al. 2012).

In some mantle silicates and oxides, dissolved water-related defects, in the form of chemically bound hydroxyl, may enhance strain rates by reducing the Peierls stress. For instance, under dry conditions the measured Peierls stress of olivine, the most abundant mineral in the Earth's upper mantle, is between 3.8 GPa (Idrissi et al. 2016) and ~15 GPa (Demouchy et al. 2013), although more typical values are in the range 5-10 GPa (eg. Evans and Goetze 1979; Kranjc et al. 2016;

66 Proietti et al. 2016). In contrast, high-stress, low-temperature deformation experiments designed to
67 measure the Peierls stress of hydrated olivine report its value to be in the range 1.6-2.9 GPa
68 (Katayama and Karato 2008), significantly below the range of Peierls stresses measured for dry
69 olivine. These experiments have measured only an average Peierls stress for olivine, which does not
70 correspond to any individual slip system. However, changes in the deformation fabric with water
71 content suggest that some slip systems are more sensitive to water content than others (Jung and
72 Karato 2001; Katayama et al. 2004).

73 In pure MgO, hydrogen is incorporated via the charge-neutral substitution of an Mg^{2+} ion by a pair
74 of protons, represented in the Kroger-Vink notation as $\{2H_{Mg}\}^{X}$ (Kroger and Vink 1956).
75 Analogous defects, in which a divalent cation (typically Mg or Fe) is replaced with two protons are
76 also found in (Mg, Fe)-silicates in the mantle, including olivine (Bai and Kohlstedt 1993; Kohlstedt
77 et al. 1996). The solubility of hydrogen in MgO is very low, and under conditions of ambient
78 pressure and water saturation, the concentration of hydrated Mg vacancies is <10 wt ppm H_2O
79 (Joachim et al. 2012). However, concentrations of hydrated vacancies may be much higher in
80 regions of the crystal under compressional strain, as is the case directly above the glide plane of an
81 edge dislocation. This is certainly the case for bare Mg vacancies (ie. vacancies without protons
82 present), which in cluster-based simulations segregate strongly to 1/2<110>{110} edge dislocation
83 cores in MgO, with a segregation energy of -1.7 eV for the tightest binding site (Zhang et al. 2010).
84 *Ab initio* calculations show that $\{2H_{Mg}\}^{X}$ defects in MgO bind to {310} tilt grain boundaries, which
85 can be modeled as an array of dislocation, with minimum segregation energies on the order of -1 eV
86 at 0 GPa (Karki et al 2015).

87 A number of different methods exist for calculating Peierls stresses from atomistic simulations.
88 While fully atomistic calculations are possible, one approach that has seen considerable use in

89 materials science is the Peierls-Nabarro (PN) method (Peierls 1940, Nabarro 1947). This model
90 uses a hybrid continuum-elastic approach in which a dislocation is represented as a discrete
91 distribution of dislocation density which interact with each other elastically, held together by
92 inelastic restoring forces representing the shear strength of the crystal. These restoring forces can be
93 calculated using atomistic simulations by introducing the concept of a generalized stacking fault
94 (GSF), which is a translational discontinuity across the glide plane of the crystal, whose energy can
95 be calculated using any one of the numerous atomic simulation techniques available (Christian and
96 Vítek 1979).

97 The PN approach has been applied to calculation of dislocation properties, including Peierls
98 stresses, of dislocations in pure MgO, and is able to reproduce experimentally observed dislocation
99 properties with some accuracy. Carrez et al. (2009) used an *ab initio* parameterized continuous PN
100 model of relative slip strength in MgO, predicting that the 1/2<110>{110} slip system is
101 approximately an order of magnitude weaker than the 1/2<110>{100} slip system, consistent with
102 experimental observations (eg. Foitzik et al. 1989). *Ab initio* parameterised Peierls-Nabarro-
103 Galerkin (PNG; Denoual 2004) simulations show that Peierls stress of the 1/2<110>{110} slip
104 system is lower than that of the 1/2<110>{100} slip system at low pressure, but that the strengths of
105 the two slip systems converge at lower mantle pressures (Amodeo et al. 2012). This approach was
106 used as the basis for simulations of dislocation mobility by kink-nucleation in MgO (Cordier et al.
107 2012).

108 In this study, we use the PN model to compare Peierls-stresses in MgO with and without dissolved
109 $\{2H_{Mg}\}^{X}$ defects, in order to determine whether hydrous defects can reduce the Peierls stress in
110 mantle minerals, and to determine the possible significance of this for deformation of MgO. To do
111 this, we use density functional theory (DFT; Hohenberg and Kohn, 1964; Kohn and Sham, 1965) to

112 calculate generalized stacking fault energies are calculated for slip in the 1/2<110> direction on the
113 {100} and {110} planes, with and without $\{2H_{Mg}\}^X$ defects present at the slip plane. These GSF
114 energies, together with elastic constants calculated *ab initio* are used to parameterize PN models for
115 1/2<110>{100} and 1/2<110>{100} dislocations in both hydrous and anhydrous MgO.

116 **2. Computational Details**

117 *2.1 Ab initio calculations*

118 All atomistic calculations performed in this study use plane-wave density functional theory (DFT),
119 as implemented in version 5.2.0 of Quantum Espresso (Giannozzi et al. 2009). Core and semi-core
120 electrons were represented using the planar augmented wave (PAW) method (Blöchl 1994), while
121 the exchange correlation (xc) energy was treated using the PBEsol xc-functional (Perdew et al.
122 2008). This xc-functional, which was developed to correct biases in earlier parameterizations
123 towards isolated systems, was chosen for its ability to accurately predict the structure and properties
124 of crystalline solids (see eg. Ropo et al. 2008; Demichelis et al. 2010). The PAW data sets for Mg,
125 H, and O atoms are from version 1.0.0 of `pslibrary` (Dal Corso 2014); details of their generation
126 parameters can found therein. The kinetic energy cutoff and spacing of the Monkhorst-Pack grid
127 used to sample reciprocal space (Monkhorst and Pack 1976) were chosen to ensure convergence of
128 the total energy to with <5 meV/atom. This required a kinetic energy cutoff of 80 Ry (~1090 eV)
129 and a Monkhorst-Pack grid spacing that corresponds to a 4x4x4 grid for the 8-atom rock salt unit
130 cell. In all calculations, free parameters (atomic positions and, where applicable, cell parameters)
131 were relaxed using the BFGS quasi-Newton scheme (Pfrommer et al. 1997).

132 In the bulk crystal, the lowest energy configuration of $\{2H_{Mg}\}^X$ defect is one in which the two
133 hydrogen ions are bonded to opposing oxygen ions within the M-site octahedron, with the O-H

bonds in each defect parallel and pointing towards the center of the site. This is consistent with the DFT calculations of Hernández et al. (2013), who similarly found the linear hydrogen configuration to be the most stable. There are three possible arrangements and all possible configurations of this defect are symmetry equivalent in a perfect crystal. However, as discussed below, the insertion of a topological defect such as a dislocation or generalized stacking fault breaks the symmetry of the crystal, leading to multiple symmetry-inequivalent configurations of the $\{2H_{Mg}\}^X$ defect.

The elastic constants C_{ij} determine the strength of the repulsive elastic interactions between components of the dislocation density in the PN model. These were calculated using the finite strain approach, in which a small strain is applied to the simulation cell and the internal coordinates (ie. atomic positions) are relaxed. The elastic constants can then be extracted by fitting the residual stress to the Hooke's law relation $\sigma_i = C_{ij}\epsilon_j$. Linear elasticity breaks down at large strain amplitudes whereas, if the strain amplitude is too small, the numerical error due to the use of finite convergence criteria may be of the same order as the residual stresses, leading to high uncertainties in the fitted values of the C_{ij}. The number of distinct imposed strains depends on the symmetry of the crystal; for MgO, which has cubic symmetry, a single strain was sufficient to determine all of the C_{ij}. In addition to the elastic constants of anhydrous MgO, we also calculated elastic constants for 1x1x1 and 2x2x2 supercells, each containing a single $\{2H_{Mg}\}^X$ defect, to assess the possible influence of hydrated defects on the elastic self-interaction of a Peierls-Nabarro dislocation.

2.2 Peierls-Nabarro calculations

The Peierls-Nabarro (PN) model represents a planar dislocation with finite core-width as a distribution of dislocation density ρ along the glide plane. This distribution may be continuous or discrete. The core shape is determined by the balance between the repulsive elastic interactions between components of the dislocation density distribution at different points in the crystal and the

157 inelastic restoring forces caused by the presence of a disregistry **u** in the material at the glide plane.
158 The core energy E_{CORE} of a dislocation in the PN model is

159 $$E_{CORE} = E_{ELASTIC} + E_{MISFIT} + E_{WORK}$$
160 (1)

161 where E_{MISFIT} is the inelastic energy due to displacement of atoms across the glide plane,
162 $E_{WORK} = \sigma \int u\,(x)dx$ is the work done on the dislocation by an applied stress σ, and E_{ELASTIC} is

163 $$E_{ELASTIC}[\rho(x)] = -K \iint \rho\,(x')\rho(x) ln|x - x'|dx'dx \quad (2)$$

164 which is the energy due to the elastic self-interaction of the dislocation density distribution. The
165 static core structure of the dislocation can be determined by minimizing E_{CORE} with σ = 0. The
166 Peierls stress is calculated by gradually increasing σ until equation (1) no longer has a minimum
167 energy solution, as the dislocation is able to glide freely.

168 In the classical formulation of the Peierls-Nabarro model, a dislocation core is represented as
169 continuous distribution of infinitesimal dislocation density. However, such a distribution is
170 translationally invariant, meaning that there no energy barrier to glide of the dislocation. The
171 dislocation can alternatively be represented as a distribution of dislocation density on a discrete
172 lattice (Bulatov and Kaxiras 1997). In this approach, the dislocation density takes finite values and
173 the inelastic misfit energy becomes a sum over the lattice points, ie.

174 $$E_{MISFIT} = \sum_n \gamma\left(u\left(na_p\right)\right) a_p \quad (3)$$

175 where a_{p} is the lattice spacing and $\gamma(\mathbf{u})$ (called the γ-line in 1D and the γ-surface in 2D) gives the
176 inelastic energy of a crystal lattice offset across the glide plane by **u**, the disregistry. In this work the

177 γ-line is calculated from energies recovered from generalized stacking fault calculations (Christian
178 and Vítek, 1979) with the energies calculated using density functional theory.

179 A GSF is a planar defect in a crystal across which the crystal is offset by some vector **u**,
180 perpendicular to the normal of the GSF plane. In an atomistic simulation, a GSF is inserted by
181 cutting an appropriately oriented simulation cell and displacing one half with respect to the other by
182 **u**. The atomic coordinates are then to relaxed to their minimum energy configuration, subject to the
183 constraint Mg^{2+} and O^{2-} ions can only move in the direction of the stacking fault normal. It is
184 common to incorporate a vacuum layer into the simulation cell, to prevent direct interactions
185 between stacking faults along the slab axis. In all GSF calculations described here, the vacuum
186 layer was 15 Å thick, and the coordinates of all atoms within 2.5 Å of the vacuum layer were fixed
187 during relaxation. For {100} and {110} oriented simulation cells, the energies of the γ-line maxima
188 to within 10 meV/Å^2 by the use of a slab cell whose thickness (in units of the fault normal vector) was n
189 = 6. GSF cell geometries for simulating slip on {100} and {110} are shown in Fig. 1.

190 To calculate the effect of protonated Mg vacancies on GSF energies, all γ-line calculations were
191 repeated with simulation cells containing a single $\{2H_{Mg}\}^X$ defect at the slip plane, with the cell
192 dimensions in the *x*- and *y*-directions doubled to reduce interactions between the defect and its
193 periodic images. Consistent with the fact that the strain field induced by a point defect decays more
194 quickly with distance than that of an unstable stacking fault, the slab cell thickness used in
195 calculations of GSF energies without adsorbed point defects were sufficient to ensure convergence
196 of those with $\{2H_{Mg}\}^X$ defects present at the slip plane. For the {100} GSF calculations, this
197 corresponds to a cross-sectional area of $\sqrt{2}a$x$\sqrt{2}a$, where *a* is the unit cell parameter of MgO, while
198 the cross-sectional area of the cell used in the {110} GSF calculations was $\sqrt{2}a$x2*a*. However,
199 although the differently oriented simulation cells have different cross-sectional areas, the number of

defects per lattice site at the slip plane is the same for the {100} and {110} oriented simulation cells, permitting a direct comparison of the effects of protonated Mg vacancies on glide of 1/2<110>{100} and 1/2<110>{110} dislocations.

Parameterizing the inelastic restoring force using calculations of GSF energies in which a point defect has been inserted allows us to investigate the potential influence that point defect might have on the core structure and mobility of a particular dislocation. The dislocation properties calculated using this represent only an approximation to the true effect that the point may have, as the point defect is effectively spread out across the entire dislocation core. This is less of a problem for dislocations in MgO, which have narrow, undissociated cores, than it would be for dislocations with widely dissociated cores, for example [001] dislocations in olivine (Durinck et al. 2007) and [010] dislocations in wadsleyite (Metsue et al. 2010). Additionally, because the PN model does not simulate an individual point defect, it is impossible to calculate the binding energy between the point defect and a dislocation. However, the PN model has some advantages over fully atomistic calculations, the most important of which is that GSF simulation cells contain fewer atoms than those used in fully atomistic simulations of dislocations, so that it is possible to use DFT instead of empirical potentials, which may be inaccurate for highly deformed regions of a crystal, such as in the vicinity of a dislocation core.

3. Results and Discussion

3.1 Elastic constants

The shape and mobility of a Peierls-Nabarro dislocation are controlled by the balance between the repulsive elastic interactions between components of the dislocation density and the inelastic restoring parameterized using GSF calculations. Before addressing the effects of adsorbed $\{2H_{Mg}\}^{X}$

222 defects on GSF energies, we will address the question of how sensitive the elastic constants C_{ij} -
223 and through them the elastic prefactor K in equation (2) - are to the concentration of these defects.

224 Compared with the experimental measurements (taken from Singokeikin and Bass, 1999), the
225 PBEsol xc-functional predicts modestly lower elastic stiffness, with the calculated 0 GPa elastic
226 constants less than their experimental values by 1.6% (C_{11}) and 6.9% (C_{44}). To determine the effect
227 of water on the elastic constants of MgO, we compare the C_{ij} calculated for anhydrous MgO above
228 with those calculated using 1x1x1 and 2x2x2 supercells, each containing a single $\{2H_{Mg}\}^X$ defect
229 (Table 1). In the 1x1x1 supercell, one quarter of the Mg sites are replaced with $\{2H_{Mg}\}^X$, while the
230 2x2x2 supercell contains one $\{2H_{Mg}\}^X$ per 32 Mg sites. The Voigt-Reuss-Hill average of the
231 isotropic shear modulus, G^{VRH}, for the 1x1x1 cell is ~18% softer than the dry shear modulus at 0
232 GPa, compared with a ~4% shear modulus relaxation of the shear modulus for the 2x2x2 simulation
233 cell. Pressure increases the relative shear modulus deficit of the 1x1x1 simulation cell slightly, to
234 ~19.5%, while that of the 2x2x2 simulation cell is essentially pressure invariant. However, while
235 the effect of water on the isotropic shear modulus is relatively pressure insensitive, this is not the
236 case for the individual elastic constants. For instance, the value of C_{12} for the 1x1x1 simulation cell
237 is ~34.7% lower than that of dry MgO at 0 GPa, but only 18.7% lower at 100 GPa.

238 For a more rigorous quantification of the effect of defect chemistry on the elasticity of a material,
239 we can compute the Euclidean distance between the elasticity tensors of the pure material and the
240 supercells containing protonated vacancies. To do this, the elasticity tensor is represented as a 21-
241 dimensional vector, corresponding to the number of linearly independent elastic constants C_{ij} for a
242 triclinic crystal, with appropriate prefactors to maintain invariance under coordinate transformations
243 (Browaeys and Chevrot 2004). The distance between two elasticity tensors is then $||\mathbf{C}_1-\mathbf{C}_2||$, where
244 $\mathbf{C}_1$ and $\mathbf{C}_2$ are the vector representations of the two tensors, and the relative deviation of $\mathbf{C}_1$ from $\mathbf{C}_2$

is $||\mathbf{C}_1-\mathbf{C}_2||/||\mathbf{C}_2||$. For MgO, which has cubic symmetry, only the first 9 components of the vectorial representation of the elasticity tensor are non-zero, with components 1-3 equal to C_{11}, components 4-6 equal to $\sqrt{2}C_{12}$, and components 7-9 equal to $2C_{44}$. This technique has been used to calculate the effect of chemistry and order on the elasticity of metal alloys (eg. Xie et al. 2012; Zhou et al. 2013). Using the elastic constants reported in Table 1, we calculate the normalized distance between the elasticity tensor of dry MgO and a 1x1x1 supercell to be 0.239 at 0 GPa, decreasing to 0.15 at 125 GPa. The elasticity tensor of the 2x2x2 supercell is even closer to that of dry MgO, reflecting the 8-fold reduction in the defect concentration, with a normalized distance between the dry and wet **C** of just 0.046 at ambient pressure, decreasing only slightly with pressure to 0.043 at 125 GPa.

Crystal elasticity affects the core properties of a dislocation through the elastic energy coefficient K in equation (2), which depends both on the elastic constants C_{ij} and the dislocation geometry. Elastic energy coefficients for the 1/2<110>{100} and 1/2<110>{110} edge dislocations, and for the 1/2<110> screw dislocation (whose coefficient is the same for glide on {100} and {110}) calculated from the elastic constants of dry and protonated vacancy-containing MgO. As expected, the elastic energy coefficients calculated from the elastic constants of supercells containing a $\{2H_{Mg}\}^X$ defect are systematically lower than those calculated for dislocations in dry MgO (Table 1). At 0 GPa, K_e for the 1/2<110>{100} slip system is 22.2 % lower when calculated using the elastic constants for the 1x1x1 supercell. However, the K_e for this slip system computed using the elastic constants of the 2x2x2 supercell differs form the dry value by only -4.6 %, comparable to the difference between the DFT and experimental values. The value of K_e calculated for the 1/2<110>{110} slip system at ambient pressure is even less sensitive to the concentration of $\{2H_{Mg}\}^X$ defects, with the values calculated using the elastic constants of the 1x1x1 and 2x2x2 supercells differing from the dry K_e by -13.2 % and -3.9 %, respectively. However, the deficit increases modestly with pressure, reaching -18.1 % and -4.3 % at 125 GPa. The effect of $\{2H_{Mg}\}^X$

concentration on K_s, the elastic energy coefficient of the 1/2<110> screw dislocation, is similar to that reported for K_e.

For MgO, as for magnesian silicates such as forsterite (Liu et al. 2009) and wadsleyite (Mao et al. 2008; Chang et al. 2015), the incorporation of water as protonated vacancies softens the elasticity tensor. However, this effect decreases rapidly with decreasing water content. Consequently, since the simulation cells used for GSF calculations in this study have relatively large cross-sections and bulk water solubilities are extremely low in both MgO (<10 ppmw; Joachim et al. 2012) and (Mg, Fe)O (<100 ppmw; Bolfan-Casanova et al. 2003), the elastic energy coefficients for all PN simulations in this study were calculated using the elastic constants of dry MgO.

3.2 Generalized stacking fault energies

To determine the effect of $\{2H_{Mg}\}^X$ defects on inelastic stacking faults in MgO, it is first necessary to calculate the energies of these stacking faults in the absence of adsorbed point defects (shown in Fig. 2). At 0 GPa, the maximum energy computed along the 1/2<110> γ-line is associated with the 1/4<110> stacking fault vector for slip on both the {110} and {100} families of of planes, with values of 0.0691 eV/Å^2 and 0.1434 eV/Å^2, comparable to the values of 0.0655 and 0.1361 eV/Å^2 calculated for these GSFs using the PBE xc-functional in a previous study (Carrez et al. 2009). However, {110} GSF energies are more pressure sensitive than {100} GSF energies. Comparing the energies of the 1/4<110> stacking fault vector on {110} and {100} as functions of pressure (Fig. 3), it can be seen that, in the former case, the calculated GSF energy increases almost six-fold over the pressure range 0-125 GPa, reaching 0.3907 eV/Å^2 at the highest pressure, whereas the energy of the 1/4<110> stacking vector on {100} is roughly doubled, reaching 0.2605 eV/Å^2 at 125 GPa. This causes a reversal of the relative heights of the 1/2<110>{110} and 1/2<110>{100} γ-lines, which occurs at ~54 GPa. Since the γ-line functions influence the dislocation energy

(equation 1) through the inelastic misfit energy (equation 3), this means that the relative strengths for dislocation glide on {110} and {100} will invert at high pressure.

Due to the high symmetry of MgO, there are three possible symmetry equivalent – and thus energy degenerate – configurations of the $\{2H_{Mg}\}^X$ defect in the bulk crystal. However, this energy degeneracy is lifted by the insertion of a stacking fault. There are two distinct configurations of the $\{2H_{Mg}\}^X$ defect for GSFs on {110}. In one, the O-H bonds lie within the stacking fault plane, but are normal to the stacking fault vector (Fig. 4a). For the other, the O-H bonds intersect the glide plane with an angle of 45° (Fig. 4b). There are likewise two symmetrically distinct configurations for a protonated vacancy located near the {100} plane: one with the O-H bonds in the fault plane and inclined 45° with respect to the GSF vector (Fig. 4c), and the other with O-H bonds normal to the fault plane (Fig. 4d). For both {100} and {110} oriented fault planes, the configuration whose O-H bonds are make an angle of 45° with respect to 1/2<110> is doubly degenerate.

The orientation of the O-H bonds in the $\{2H_{Mg}\}^x$ defect, relative to the slip plane, influences the calculated GSF energy, as can be seen by comparing the wet and dry γ-lines (Fig. 2). For slip on {110}, the defect configuration in which the O-H bonds cross the slip plane has a γ-line maximum of 0.0923 eV/Å^2, higher than the calculated γ-line maximum for dry MgO. In contrast, the γ-line maximum is reduced by the presence of the defect with the O-H bonds within the {110} plane, to just 0.0529 eV/Å^2. At 125 GPa applied pressure, the corresponding values for the two defect configurations are 0.3572 and 0.3423 eV/Å^2. For slip on {100}, meanwhile, the γ-line maximum at 0 GPa is 0.1447 eV/Å^2 when O-H bonds are aligned normal to the glide plane compared with 0.1214 eV/Å^2 when the O-H bonds are parallel to it. At 125 GPa, the corresponding energies are 0.2378 eV/Å^2 and 0.2194 eV/Å^2 so that, while the absolute and relative differences in energy are reduced, the defect with O-H bonds in the slip plane remains lower in energy. In summary, for slip

315 along 1/2<110> on {110} and {100}, it is clear that the orientation of the O-H bonds relative to the
316 slip plane influences the degree of water weakening, with lower energies when the configuration of
317 the adsorbed $\{2H_{Mg}\}^X$ defect has O-H bonds parallel to the slip plane. In the following section,
318 where we calculate Peierls stresses for dislocations in hydrous MgO, we will use the γ-lines
319 calculated for these $\{2H_{Mg}\}^X$ defects.

320 One way to quantify the impact of a protonated vacancy on a generalized stacking fault is to
321 consider the relative reduction of the γ-line maximum by the addition of a single defect at the
322 stacking fault plane. For the 1/2<110>{110} γ-line, the energy maximum at 0 GPa is reduced by
323 23% by the addition of a $\{2H_{Mg}\}^X$ defect, the deficit decreasing steadily with pressure to 12% at
324 125 GPa. In contrast, the 1/2<110>{100} γ-line is less affected by the presence of a protonated
325 defect at 0 GPa, and the maximum energy decreases by 15%. However, the relative magnitude of
326 the γ-line relaxation increases slightly with pressure, to 16% at 125 GPa.

327 As mentioned at the end of section 2.2, it is impossible to calculate the binding energy between a
328 point defect and a dislocation with the PN formalism. However, by taking the difference between
329 dry and wet GSF energies with the same stacking fault vector **u**, it possible to determine the
330 segregation energy E_{seg} of a protonated vacancy from the bulk to a generalized stacking fault. For
331 the 1/4<110>{100} GSF, the segregation energy at 0 GPa is -0.78 eV, rising to -1.14 eV at 125
332 GPa. At 0 GPa, the segregation energy to a 1/4<110>{110} GSF is -0.81 eV, but rises more quickly
333 with pressure, reaching -1.90 eV at 125 GPa. While a direct quantitative comparison with the results
334 of Karki et al (2015) for $\{2H_{Mg}\}^X$ segregation to {310} tilt boundaries is not possible, the
335 magnitudes of the segregation energies reported at 0 GPa in that study are comparable to those
336 found here (approximately -1 eV), and increase with pressure.

337 *3.3 Peierls-Nabarro dislocations*

Using the γ-lines calculated in section 3.2, Peierls-Nabarro dislocation core structures can be obtained by minimizing equation (1) with applied stress $\sigma = 0$. A static dislocation can be characterized by its core width ξ, which is defined to be the width of the region within which $|\mathbf{b}|/4 < |\mathbf{u}(x)| < 3|\mathbf{b}|/4$, and its maximum dislocation density, ρ_{max}. In anhydrous MgO, both of these parameters are nearly constant for the 1/2<110>{100} edge dislocation and the 1/2<110> screw dislocation spreading on {100}, whereas ξ and ρ_{max} respectively decrease and increase for the 1/2<110>{110} edge dislocation and the 1/2<110> screw dislocation spreading on {110} (Fig. 5). Relaxing the static dislocation core structure using the wet γ-lines increases core spreading, particularly on the {110} plane, with a corresponding decrease in the value ρ_{max}. However, this hydrogen-induced dislocation core spreading has no significant effect on the pressure derivatives of either ξ or ρ_{max}.

From these static dislocation core structures, Peierls stresses for the different slip systems can be obtained by minimizing equation (1) with $|\sigma| > 0$, using the static disregistry profile $\mathbf{u}(x)$ as input. Within the 1/2<110>{110} slip system, the Peierls stress of the 1/2<110>{110} edge dislocation is lower than that of the 1/2<110> screw dislocation gliding on {100}, which controls mobility in this slip system. The Peierls stress of the edge dislocation at ambient pressure is 0.06 GPa, similar to the 0.02 GPa (Carrez et al. 2009) and 0.04 GPa (Liu et al. 2012) calculated for this dislocation in previous studies. For the 1/2<110> screw dislocation, σ_p for glide on {110} is 0.26 GPa at ambient pressure. Previous computational studies have found values for this slip system ranging from 0.04 GPa (Carrez et al. 2009) to 0.16 GPa (Liu et al. 2012). For the 1/2<110>{100} slip system we find that, across the entire pressure range 0-125 GPa, a 1/2<110> screw dislocation gliding on {100} has lower Peierls stress than 1/2<110>{100} edge dislocation. At 0 GPa, the screw dislocation has σ_p = 1.7 GPa for the screw dislocation, comparable to the value of 1.53 GPa calculated by Carrez et al.

(2009) using a continuous 1D PN model. Carrez et al. determined the Peierls stress of the 1/2<110>{100} edge dislocation at ambient pressure to be 1.16 GPa, markedly lower than the 2.8 GPa computed in this study.

The 0 GPa Peierls stresses are thus comparable with those found in previous studies, albeit modestly higher for all dislocations studied. This difference can be attributed to the choice of xc-functional as Carrez et al. (2009) and Liu et al. (2012) used the PBE-GGA xc-functional (Perdew et al. 1996), which is known to significantly overestimate the cell volume, due to under-binding of the exchange-correlation energy. For MgO, the elastic constants C_{ij} increase with decreasing cell volume (ie. increasing pressure) which means that, at a given pressure the PBE xc-functional underestimates the elastic constants. Consequently, PN simulations parameterized using the results of DFT calculations performed using the PBE xc-functional should consistently predict lower Peierls stresses than those parameterized using the PBEsol xc-functional, as is the case here.

In section 3.2, it was shown that adsorption of $\{2H_{Mg}\}^X$ defects to the fault plane lowers GSF energies along the 1/2<110>{110} γ-line. When these γ-lines are used to parameterize PN calculations of dislocation glide, this translates into lower Peierls stresses for glide on the 1/2<110>{110} slip system. Although the edge and screw dislocations in this slip have comparable Peierls stresses at ambient pressure, above 0 GPa the Peierls stress of the 1/2<110> screw dislocation gliding on {110} is greater than that of the 1/2<110>{110} edge dislocation, and screw dislocation controls the mobility of this slip system. At 0 GPa, the Peierls stress of a 1/2<110>{110} edge dislocation is 0.06 GPa, indistinguishable from the Peierls stress for this slip system in dry MgO. However, as can be seen in Fig. 6(a), the pressure derivative $d\sigma_p/dP$ is lowered by $\{2H_{Mg}\}^X$ defects and, at 125 GPa pressure, the σ_p calculated using the wet γ-line is 1.7 GPa, <50% of the value for this dislocation in dry MgO (3.6 GPa). For glide of 1/2<110> screw

384 dislocations on {110}, the Peierls stress is 0.06 GPa when the wet γ-line is used, compared with
385 0.26 GPa under dry conditions; at 125 GPa the corresponding wet and dry values are 10.6 and 23.0
386 GPa.

387 The effect of protonated vacancies on the qualitative pressure dependence of dislocations gliding on
388 {100} is more pronounced. Whereas, in dry MgO, the Peierls stress of 1/2<110>{100} edge
389 dislocations increases monotonically with pressure, the addition of water leads to a pronounced
390 negative curvature of $\sigma_p(P)$. This effect is sufficiently great that σ_p actually decreases above 75
391 GPa. The Peierls stress for glide of 1/2<110> screw dislocations on {100} is similar for anhydrous
392 and hydrous MgO at ambient pressure (~1.7 GPa). However, the adsorption of protonated vacancies
393 to the glide plane greatly reduces the pressure dependence of σ_p, which in hydrous MgO is just 2.7
394 GPa at 125 GPa, compared with 4.2 GPa for dry MgO. As was found for dry MgO, the Peierls
395 stress of the 1/2<110>{100} dislocation is greater than that of the 1/2<110> screw dislocation
396 gliding on {100} at all pressures, although in wet MgO the Peierls stress for the edge and screw
397 dislocation begin to converge at high pressure.

398 For 1/2<110> screw dislocations in dry MgO, the relatively rapid increase in σ_p for glide on {110}
399 with pressure means that glide on {100} becomes easier at high pressure. This results in a cross-
400 over of the relative strengths of the two glide planes at high pressure. Using the Peierls stresses
401 calculated for dry MgO, we that this occurs at a pressure of 24.8 GPa, comparable to the ~23 GPa
402 measured in creep experiments (Girard et al. 2012). However, glide of 1/2<110> screw dislocations
403 on {110} is preferentially enhanced by the presence of protonated vacancies over glide on {100}.
404 While this effect is not sufficient to prevent the preferred glide plane from changing at mantle
405 pressures, the slip system cross-over is shifted to higher pressures (Fig. 7b). For the $\{2H_{Mg}\}^X$ defect
406 concentrations used in this study, the cross-over pressure at which glide of 1/2<110> screw

dislocation on {110} increases to 32.1 GPa. Assuming linear dependence of the Peierls stress on $\{2H_{Mg}\}^X$ defect, this implies that the cross-over pressure is shifted by ~29 GPa multiplied by the fraction of protonated cation sites at the glide plane. In anhydrous MgO, the 1/2<110>{110} edge dislocation slip system is weaker than the 1/2<110>{100} edge dislocation slip system at all mantle-relevant pressures (Fig. 7a), and this is not changed by the incorporation of $\{2H_{Mg}\}^X$ defects at the glide plane. However, the pressure at which the Peierls stress of 1/2<110> screw dislocation on {110} exceeds that of the 1/2<110>{100} edge dislocation increases from 30.6 GPa in dry MgO to 46.2 GPa for hydrous MgO with $\{2H_{Mg}\}^X$ present at the concentrations used in this study, giving a dependence of the cross-over pressure on $\{2H_{Mg}\}^X$ concentration of ~62 GPa times the fraction of occupied sites.

The hydrolytic weakening of the Peierls stress found here is a direct result of the reduction of the γ-line maximum by the insertion of suitably oriented $\{2H_{Mg}\}^X$ defects at the slip plane. This reduces the inelastic restoring force that balances the repulsive elastic interaction between components of the dislocation density distribution ρ at different lattice planes. What cannot be determined, however, is whether the reduction of the γ-line energies is due to the presence of hydrogen, or the vacancy generated when creating a $\{2H_{Mg}\}^X$ defect. Given that the 1/2<110> γ-line maxima on both {110} and {100} correspond to the points of closest approach between Mg atoms on either side of the stacking fault plane, it is likely that the mechanism by which protonated vacancies reduce the Peierls stress is by minimizing the repulsive interactions between adjacent Mg ions across the glide plane. In this case, the role of the H atoms is solely to charge-balance the creation of an Mg vacancy.

Creation of protonated defects is not the only mechanism by which vacancies can be generated in MgO or its iron-bearing analogue (Mg, Fe)O. Insertion of trivalent cations, such as Al^{3+} and Fe^{3+}

430 into MgO/(Mg, Fe)O leads to the creation of M-site vacancies to maintain overall charge neutrality.
431 Extrinsic vacancies associated with trivalent cations can vastly outnumber intrinsic vacancies, such
432 as those associated with Schottky defects (Van Orman et al. 2009). In the case of MgO, doping with
433 trivalent cations at the 100-200 ppm level decreases dislocation mobility and increases its critical
434 resolved shear stress (Singh and Coble 1974ab). The increase in yield strength is nearly identical for
435 Cr^{3+}, Al^{3+}, and Fe^{3+}, despite their different ionic radii, which suggests that this pinning is not caused
436 by attractive elastic interactions between the trivalent cation and the dislocation core but the
437 substantial change in the electrostatic energy of this complex when it is sheared by a passing
438 dislocation (Ahlquist 1975). However, Otsuka et al. (2010) have suggested that under lower mantle
439 conditions, ferric iron and $\{\square_M\}''$ vacancies dissociate. It is thus possible that, under oxidized
440 conditions, there will be free vacancies, capable of inducing Peierls stress reductions comparable to
441 those predicted here for protonated vacancies to dislocation cores, with similar geophysical
442 implications. More work needs to be done to investigate the effects of Fe^{3+} on the deformation of
443 (Mg, Fe)O with realistic Fe contents.

444 Iron-bearing (Mg, Fe)O is the weakest major phase in the Earth's lower mantle. In both numerical
445 simulations of two-phase creep (Madi et al. 2005) and high-pressure deformation experiments on
446 magnesiowustite + bridgmanite aggregates (Girard et al. 2016) the bulk of the strain in multi-phase
447 lower mantle materials is accommodated by (Mg, Fe)O. When deformed under moderate stress
448 conditions, (Mg, Fe)O polycrystals develop pronounced lattice preferred orientation (LPO)
449 (Yamazaki and Karato 2002), although a recent deformation experiment of a magnesiowustite +
450 bridgmanite at 61 GPa found no evidence for the development of a coherent deformation fabric
451 (Miyagi and Wenk 2016). MgO is highly elastically anisotropic over the entire pressure range of the
452 Earth's mantle (Karki et al. 1999). (Mg, Fe)O is even more anisotropic than pure MgO and probably
453 accounts for the majority of the observed seismic wave anisotropy in the Earth's lower mantle

454 (Marquardt et al. 2009), especially as (Mg, Fe)SiO_3 bridgmanite, the other major component of the
455 lower mantle, does not develop any significant LPO when deformed under mantle-relevant
456 conditions (Merkel et al. 2003). At high pressure, the 1/2<110> screw dislocations experience more
457 lattice friction for glide on {110} than on {100}, which results in a change in the LPO for a give
458 pattern of mantle strain. Lattice preferred orientation of (Mg, Fe)O has also been invoked to explain
459 seismic anisotropy in the D″ region of the lowermost mantle, on the assumption that the dominant
460 slip system is 1/2<110>{100} (Karato 2014). In hydrous MgO, the greatest Peierls stress reduction
461 was found for the 1/2<110>{110} slip system, so that the pressure at which {100} becomes the
462 dominant slip for the 1/2<110> screw dislocations is displaced to higher pressures under hydrous
463 conditions. At pressures representative of the deep lower mantle, the preferred slip system is the
464 same for both hydrous and anhydrous MgO. However, $\{2H_{Mg}\}^X$ defects preferentially enhance
465 1/2<110>{110} slip by $\{2H_{Mg}\}^X$ defects, thereby altering the relative activities of the two major
466 slip systems in MgO and changing its LPO, and potentially the observed pattern of seismic
467 anisotropy.

468 **Conclusions**

469 In this study, we have used the PN model, parameterized using *ab initio* calculated GSF energies to
470 determine the effect of a common variety of protonated vacancy, $\{2H_{Mg}\}^X$, on the Peierls stress of
471 MgO. Using DFT, 1/2<110> γ-lines were calculated for slip on the {110} and {100} families of
472 planes, representing the most important slip systems in MgO, and these were used to parameterize
473 Peierls-Nabarro calculations of edge and screw dislocation core structures and Peierls stresses.
474 Calculations were performed using stoichiometric MgO simulation cells, in addition to simulation
475 cells containing $\{2H_{Mg}\}^X$ defects, and it was found that the latter produced wider dislocation cores
476 and lower Peierls stresses over the entire pressure range of the Earth's mantle. Although σ_p is

decreased by the presence of protonated vacancies at the glide plane for slip on both {100} and {110}, we find that the Peierls stress reduction is greatest for 1/2<110>{110} slip (for both edge and screw dislocations). In the case of 1/2<110> screw dislocations, this leads to an increase in the pressure at which glide on {100} becomes easiest, meaning that the presence of water may influence the deformation fabric.

These calculations show that the presence of protonated defects near a dislocation core in MgO can reduce its Peierls stress. However, although we have considered only MgO, the results have implications for the glide controlled creep of other mantle minerals such as olivine or pyroxene. The easy glide planes of the dominant slip systems for dislocation are parallel to sheets of MO_6 octahedra (where M is typically Mg or Fe), for which MgO may be considered a structurally simple analogue. Glide lubrication by protonated defects may provide an explanation for the lower yield strength and different LPO of hydrous versus anhydrous olivine, and this possibility warrants further exploration using atomistic simulations.

Acknowledgements

AMW is grateful for support from the UK Natural Environment Research Council (NE/K008803/1 and NE/M000044/1). RS is supported by an Australian Government Research Training Program (RTP) Scholarship. Calculations were performed on the Terrawulf cluster, a computational facility supported through the AuScope initiative. AuScope Ltd is funded under the National Collaborative Research Infrastructure Strategy (NCRIS), an Australian Commonwealth Government Programme. This work used the ARCHER UK National Supercomputing Service (http://www.archer.ac.uk). The authors would like to thank Ph. Carrez and an anonymous reviewer for thoughtful comments, which greatly improved the clarity and quality of the manuscript.

499 **References**

500 Ahlquist CN (1975) Solution strengthening of MgO crystals. Journal of Applied Physics 46:14–17 .
501 doi: 10.1063/1.322198

502 Amodeo J, Carrez P, Cordier P (2012) Modelling the effect of pressure on the critical shear stress of
503 MgO single crystals. Philosophical Magazine 92:1523–1541. doi: 10.1080/14786435.2011.652689

504 Asadi E, Zaeem MA, Moitra A, Tschopp MA (2014) Effect of vacancy defects on generalized
505 stacking fault energy of fcc metals. J Phys: Condens Matter 26:115404. doi: 10.1088/0953-
506 8984/26/11/115404

507 Ashbee KHG, Yust CS (1982) A mechanism for the ease of slip in UO2+x. Journal of Nuclear
508 Materials 110:246–250. doi: 10.1016/0022-3115(82)90152-0

509 Bai Q, Kohlstedt DL (1993) Effects of chemical environment on the solubility and incorporation
510 mechanism for hydrogen in olivine. Phys Chem Minerals 19:460–471. doi: 10.1007/BF00203186

511 Blöchl PE (1994) Projector augmented-wave method. Phys Rev B 50:17953–17979. doi:
512 10.1103/PhysRevB.50.17953

513 Bolfan-Casanova N, Keppler H, Rubie DC (2003) Water partitioning at 660 km depth and evidence
514 for very low water solubility in magnesium silicate perovskite. Geophys Res Lett 30:1905. doi:
515 10.1029/2003GL017182

516 Browaeys JT, Chevrot S (2004) Decomposition of the elastic tensor and geophysical applications.
517 Geophys J Int 159:667–678. doi: 10.1111/j.1365-246X.2004.02415.x

518 Bulatov VV, Kaxiras E (1997) Semidiscrete Variational Peierls Framework for Dislocation Core
519 Properties. Phys Rev Lett 78:4221–4224. doi: 10.1103/PhysRevLett.78.4221

520 Carrez P, Ferré D, Cordier P (2009) Peierls–Nabarro modelling of dislocations in MgO from
521 ambient pressure to 100 GPa. Modelling Simul Mater Sci Eng 17:35010. doi: 10.1088/0965-
522 0393/17/3/035010

523 Chang Y-Y, Jacobsen SD, Bina CR, et al. (2015) Comparative compressibility of hydrous
524 wadsleyite and ringwoodite: Effect of H2O and implications for detecting water in the transition
525 zone. J Geophys Res Solid Earth 120:2015JB012123. doi: 10.1002/2015JB012123

526 Christian JW, Vítek V (1970) Dislocations and stacking faults. Rep Prog Phys 33:307. doi:
527 10.1088/0034-4885/33/1/307

528 Cordier P, Amodeo J, Carrez P (2012) Modelling the rheology of MgO under Earth/'s mantle
529 pressure, temperature and strain rates. Nature 481:177–180. doi: 10.1038/nature10687

530 Cottrell AH, Bilby BA (1949) Dislocation Theory of Yielding and Strain Ageing of Iron. Proc Phys
531 Soc A 62:49. doi: 10.1088/0370-1298/62/1/308

532 Dal Corso A (2014) Pseudopotentials periodic table: From H to Pu. Computational Materials
533 Science 95:337–350. doi: 10.1016/j.commatsci.2014.07.043

534 Demichelis R, Civalleri B, D'Arco P, Dovesi R (2010) Performance of 12 DFT functionals in the
535 study of crystal systems: Al2SiO5 orthosilicates and Al hydroxides as a case study. Int J Quantum
536 Chem 110:2260–2273. doi: 10.1002/qua.22574

537 Demouchy S, Tommasi A, Boffa Ballaran T, Cordier P (2013) Low strength of Earth's uppermost
538 mantle inferred from tri-axial deformation experiments on dry olivine crystals. Physics of the Earth
539 and Planetary Interiors 220:37–49. doi: 10.1016/j.pepi.2013.04.008

540 Denoual C (2004) Dynamic dislocation modeling by combining Peierls Nabarro and Galerkin
541 methods. Phys Rev B 70:24106. doi: 10.1103/PhysRevB.70.024106

542 Durinck J, Carrez P, Cordier P (2007) Application of the Peierls-Nabarro model to dislocations in
543 forsterite. European Journal of Mineralogy 19:631–639 . doi: 10.1127/0935-1221/2007/0019-1757

544 Evans B, Goetze C (1979) The temperature variation of hardness of olivine and its implication for
545 polycrystalline yield stress. J Geophys Res 84:5505–5524. doi: 10.1029/JB084iB10p05505

546 Foitzik A, Skrotzki W, Haasen P (1989) Correlation between microstructure, dislocation
547 dissociation and plastic anisotropy in ionic crystals. Materials Science and Engineering: A 113:399–
548 407. doi: 10.1016/0921-5093(89)90326-2

549 Giannozzi P, Baroni S, Bonini N, et al. (2009) QUANTUM ESPRESSO: a modular and open-
550 source software project for quantum simulations of materials. J Phys: Condens Matter 21:395502.
551 doi: 10.1088/0953-8984/21/39/395502

552 Girard J, Jihua C, Raterron P (2012) Deformation of periclase single crystals at high pressure and
553 temperature: Quantification of the effect of pressure on slip-system activities. Journal of Applied
554 Physics 111:112607 . doi: 10.1063/1.4726200

555 Girard J, Amulele G, Farla R, et al. (2016) Shear deformation of bridgmanite and magnesiowüstite
556 aggregates at lower mantle conditions. Science 351:144–147. doi: 10.1126/science.aad3113

557 Hohenberg P, Kohn W (1964) Inhomogeneous Electron Gas. Phys Rev 136:B864–B871. doi:
558 10.1103/PhysRev.136.B864

559 Idrissi H, Bollinger C, Boioli F, et al. (2016) Low-temperature plasticity of olivine revisited with in
560 situ TEM nanomechanical testing. Science Advances 2:e1501671. doi: 10.1126/sciadv.1501671

561 Joachim B, Wohlers A, Norberg N, et al. (2012) Diffusion and solubility of hydrogen and water in
562 periclase. Phys Chem Minerals 40:19–27. doi: 10.1007/s00269-012-0542-8

563 Jung H, Karato S (2001) Water-Induced Fabric Transitions in Olivine. Science 293:1460–1463 .
564 doi: 10.1126/science.1062235

565 Karato S (2014) Some remarks on the origin of seismic anisotropy in the D" layer. Earth, Planets
566 and Space 50:1019. doi: 10.1186/BF03352196

567 Karki BB, Wentzcovitch RM, Gironcoli S de, Baroni S (1999) First-Principles Determination of
568 Elastic Anisotropy and Wave Velocities of MgO at Lower Mantle Conditions. Science 286:1705–
569 1707. doi: 10.1126/science.286.5445.1705

570 Karki BB, Ghosh DB, Verma AK (2015) First-principles prediction of pressure-enhanced defect
571 segregation and migration at MgO grain boundaries. American Mineralogist 100:1053–1058 . doi:
572 10.2138/am-2015-5143

573 Katayama I, Jung H, Karato S (2004) New type of olivine fabric from deformation experiments at
574 modest water content and low stress. Geology 32:1045–1048. doi: 10.1130/G20805.1

575 Katayama I, Karato S (2008) Low-temperature, high-stress deformation of olivine under water-
576 saturated conditions. Physics of the Earth and Planetary Interiors 168:125–133. doi:
577 10.1016/j.pepi.2008.05.019

578 Keller RJ, Mitchell TE, Heuer AH (1988) Plastic deformation in nonstoichiometric UO2+x single
579 crystals—I. Deformation at low temperatures. Acta Metallurgica 36:1061–1071. doi: 10.1016/0001-
580 6160(88)90160-5

581 Kohlstedt DL, Keppler H, Rubie DC (1996) Solubility of water in the α, β and γ phases of
582 (Mg,Fe)2SiO4. Contrib Mineral Petrol 123:345–357. doi: 10.1007/s004100050161

583 Kohn W, Sham LJ (1965) Self-Consistent Equations Including Exchange and Correlation Effects.
584 Phys Rev 140:A1133–A1138. doi: 10.1103/PhysRev.140.A1133

585 Kranjc K, Rouse Z, Flores KM, Skemer P (2016) Low-temperature plastic rheology of olivine
586 determined by nanoindentation. Geophys Res Lett 43:2015GL065837. doi: 10.1002/2015GL065837

587 Kröger FA, Vink HJ (1956) Relations between the Concentrations of Imperfections in Crystalline
588 Solids. Solid State Physics 3:307–435. doi: 10.1016/S0081-1947(08)60135-6

589 Lauzier J, Hillairet J, Vieux-Champagne A, Benoit W (1989) The vacancies, lubrication agents of
590 dislocation motion in aluminium. J Phys: Condens Matter 1:9273. doi: 10.1088/0953-8984/1/47/001

591 Liu L, Du J, Zhao J, et al. (2009) Elastic properties of hydrous forsterites under high pressure: First-
592 principle calculations. Physics of the Earth and Planetary Interiors 176:89–97. doi:
593 10.1016/j.pepi.2009.04.004

594 Liu L, Wu XZ, Wang R, et al. (2012) High-pressure effect on elastic constants, stacking fault
595 energy and correlation with dislocation properties in MgO and CaO. Eur Phys J B 85:1–10. doi:
596 10.1140/epjb/e2012-30032-4

597 Lu G, Zhang Q, Kioussis N, Kaxiras E (2001) Hydrogen-Enhanced Local Plasticity in Aluminum:
598 An Ab Initio Study. Phys Rev Lett 87:95501. doi: 10.1103/PhysRevLett.87.095501

599 Lu G, Kaxiras E (2002) Can Vacancies Lubricate Dislocation Motion in Aluminum? Phys Rev Lett
600 89:105501. doi: 10.1103/PhysRevLett.89.105501

601 Madi K, Forest S, Cordier P, Boussuge M (2005) Numerical study of creep in two-phase aggregates
602 with a large rheology contrast: Implications for the lower mantle. Earth and Planetary Science
603 Letters 237:223–238. doi: 10.1016/j.epsl.2005.06.027

604 Mao Z, Jacobsen SD, Jiang F, et al. (2008) Single-crystal elasticity of wadsleyites, β-Mg2SiO4,
605 containing 0.37–1.66 wt.% H2O. Earth and Planetary Science Letters 266:78–89. doi:
606 10.1016/j.epsl.2007.10.045

607 Marquardt H, Speziale S, Reichmann HJ, et al. (2009) Elastic Shear Anisotropy of Ferropericlase in
608 Earth's Lower Mantle. Science 324:224–226. doi: 10.1126/science.1169365

609 Merkel S, Wenk HR, Badro J, et al. (2003) Deformation of (Mg0.9,Fe0.1)SiO3 Perovskite
610 aggregates up to 32 GPa. Earth and Planetary Science Letters 209:351–360. doi: 10.1016/S0012-
611 821X(03)00098-0

612 Metsue A, Carrez P, Denoual C, et al (2010) Plastic deformation of wadsleyite: IV Dislocation core
613 modelling based on the Peierls–Nabarro–Galerkin model. Acta Materialia 58:1467–1478 . doi:
614 10.1016/j.actamat.2009.10.047

615 Miyagi L, Wenk H-R (2016) Texture development and slip systems in bridgmanite and bridgmanite
616 + ferropericlase aggregates. Phys Chem Minerals 43:597–613 . doi: 10.1007/s00269-016-0820-y

617 Monkhorst HJ, Pack JD (1976) Special points for Brillouin-zone integrations. Phys Rev B 13:5188–
618 5192. doi: 10.1103/PhysRevB.13.5188

619 Nabarro FRN (1947) Dislocations in a simple cubic lattice. Proc Phys Soc 59:256. doi:
620 10.1088/0959-5309/59/2/309

621 Otsuka K, McCammon CA, Karato S (2010) Tetrahedral occupancy of ferric iron in (Mg,Fe)O:
622 Implications for point defects in the Earth's lower mantle. Physics of the Earth and Planetary
623 Interiors 180:179–188. doi: 10.1016/j.pepi.2009.10.005

624 Peierls R (1940) The size of a dislocation. Proc Phys Soc 52:34. doi: 10.1088/0959-5309/52/1/305

625 Perdew JP, Burke K, Ernzerhof M (1996) Generalized Gradient Approximation Made Simple. Phys
626 Rev Lett 77:3865–3868. doi: 10.1103/PhysRevLett.77.3865

627 Perdew JP, Ruzsinszky A, Csonka GI, et al. (2008) Restoring the Density-Gradient Expansion for
628 Exchange in Solids and Surfaces. Phys Rev Lett 100:136406. doi:
629 10.1103/PhysRevLett.100.136406

630 Pfrommer BG, Côté M, Louie SG, Cohen ML (1997) Relaxation of Crystals with the Quasi-Newton
631 Method. Journal of Computational Physics 131:233–240. doi: 10.1006/jcph.1996.5612

632 Proietti A, Bystricky M, Guignard J, et al. (2016) Effect of pressure on the strength of olivine at
633 room temperature. Physics of the Earth and Planetary Interiors 259:34–44. doi:
634 10.1016/j.pepi.2016.08.004

635 Ropo M, Kokko K, Vitos L (2008) Assessing the Perdew-Burke-Ernzerhof exchange-correlation
636 density functional revised for metallic bulk and surface systems. Phys Rev B 77:195445. doi:
637 10.1103/PhysRevB.77.195445

638 Shen P, Feng H, Wu X, et al. (2015) The Core Structure and Peierls Stress of 〈 11 2 ¯ 0 〉
639 Dislocations in MgB2 with Mg and B Vacancies. J Supercond Nov Magn 28:1743–1748. doi:
640 10.1007/s10948-015-3001-1

641 Singh RN, Coble RL (1974a) Dynamic dislocation behavior in ``pure'' magnesium oxide single
642 crystals. Journal of Applied Physics 45:981–989 . doi:10.1063/1.1663445

643 Singh RN, Coble RL (1974b) Dynamic dislocation behavior in iron□doped magnesium oxide
644 crystals. Journal of Applied Physics 45:990–995 . doi: 10.1063/1.1663446

645 Sinogeikin SV, Bass JD (1999) Single-crystal elasticity of MgO at high pressure. Phys Rev B
646 59:R14141–R14144. doi: 10.1103/PhysRevB.59.R14141

647 Taketomi S, Matsumoto R, Miyazaki N (2008) Atomistic simulation of the effects of hydrogen on
648 the mobility of edge dislocation in alpha iron. J Mater Sci 43:1166–1169. doi: 10.1007/s10853-007-
649 2364-5

650 Van Orman JA, Fei Y, Hauri EH, Wang J (2003) Diffusion in MgO at high pressures: Constraints
651 on deformation mechanisms and chemical transport at the core-mantle boundary. Geophys Res Lett
652 30:1056. doi: 10.1029/2002GL016343

653 Van Orman JA, Li C, Crispin KL (2009) Aluminum diffusion and Al-vacancy association in
654 periclase. Physics of the Earth and Planetary Interiors 172:34–42. doi: 10.1016/j.pepi.2008.03.008

655 Xie M-Y, Tasnádi F, Abrikosov IA, et al. (2012) Elastic constants, composition, and piezolectric
656 polarization in InxAl1−xN: From ab initio calculations to experimental implications for the
657 applicability of Vegard's rule. Phys Rev B 86:155310. doi: 10.1103/PhysRevB.86.155310

658 Yamazaki D, Karato S (2002) Fabric development in (Mg,Fe)O during large strain, shear
659 deformation: implications for seismic anisotropy in Earth's lower mantle. Physics of the Earth and
660 Planetary Interiors 131:251–267. doi: 10.1016/S0031-9201(02)00037-7

661 Zhang F, Walker AM, Wright K, Gale JD (2010) Defects and dislocations in MgO: atomic scale
662 models of impurity segregation and fast pipe diffusion. J Mater Chem 20:10445–10451. doi:
663 10.1039/C0JM01550D

664 Zhou L, Holec D, Mayrhofer PH (2013) First-principles study of elastic properties of cubic
665 Cr1−xAlxN alloys. Journal of Applied Physics 113:43511. doi: 10.1063/1.4789378

666

667

668 **Tables**

669 **Table 1.** Calculated elastic constants (in GPa) of anhydrous MgO, compared with those of 1x1x1
670 and 2x2x2 supercells containing a single $\{2H_{Mg}\}^X$ defect. Measured elastic constants of dry MgO at
671 ambient pressure given for reference. For each set of elastic constants, we have computed the elastic
672 energy coefficients for 1/2<110>{100} and 1/2<110>{110} dislocations. While the edge
673 coefficients (K_e) differ between the two slip systems, the screw energy coefficient (K_s) does not.

		C_{11}	C_{12}	C_{44}	G^{VRH}	K_e		K_s
						1/2<110>{100}	1/2<110>{110}	
anhydrous (DFT)	0 GPa	293.2	89.8	143.8	125.1	160.7	147.7	120.9
	125 GPa	1281.5	253.1	204.7	299.0	381.2	446.1	324.4
anhydrous (expt.)[a]	0 GPa	297.9(15)	95.8(10)	154.4(20)	130.2(1)	168.8	152.0	124.9
1x1x1 supercell	0 GPa	277.8	58.6	98.1	102.6	125.0	128.2	103.7
	125 GPa	1112.3	205.8	153.1	240.7	306.1	365.3	263.4
2x2x2 supercell	0 GPa	283.6	85.3	135.8	119.7	153.3	142.0	116.0
	125 GPa	1224.7	246.6	196.3	285.8	365.2	426.7	309.8

674 [a] Sinogeikin and Bass (1999)

675 **Figure Captions**

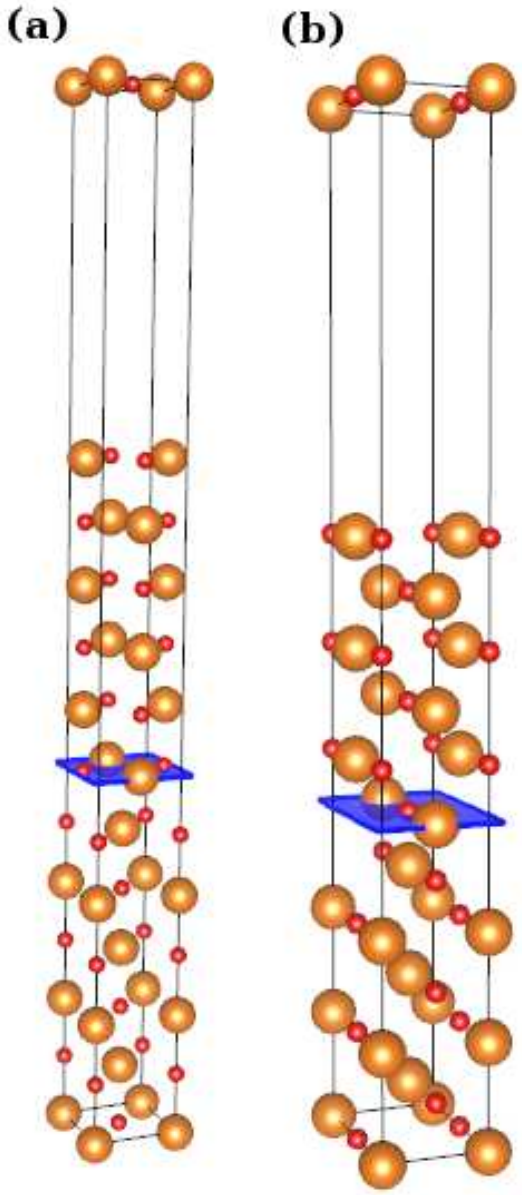

676

677 **Fig. 1** Simulation cells containing 1/4<110> generalized stacking faults on the (a) {100} and (b)

678 {110} planes.

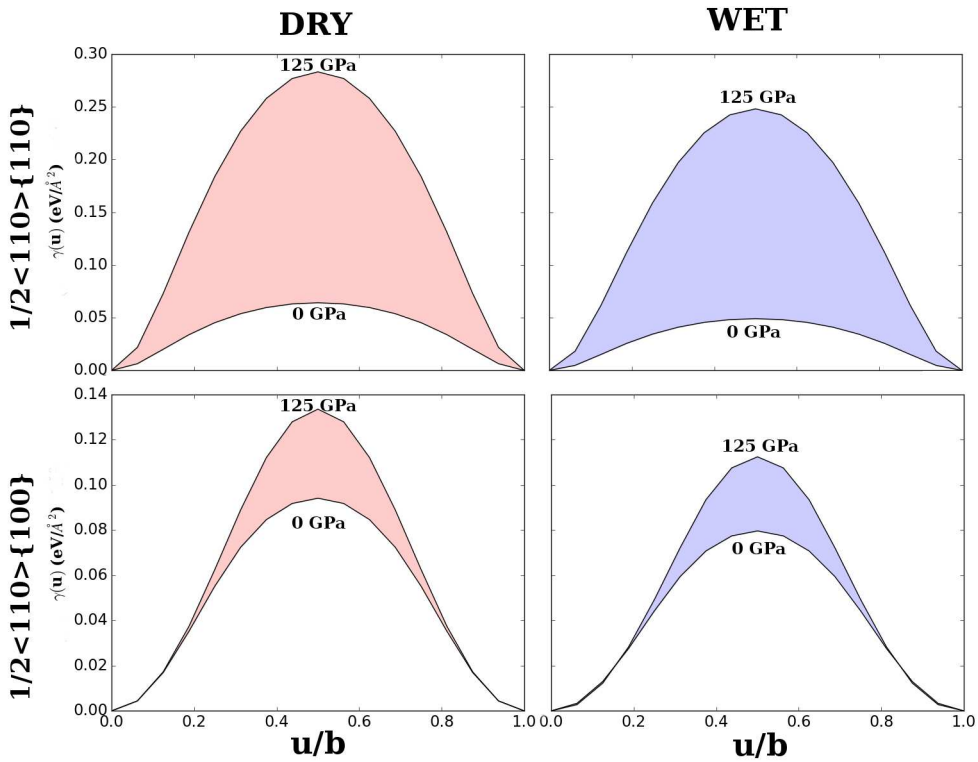

679

680 **Fig. 2** Pressure evolution of wet and dry 1/2<110>{110} (top) and 1/2<110>{100} (bottom) γ-lines

681 in MgO.

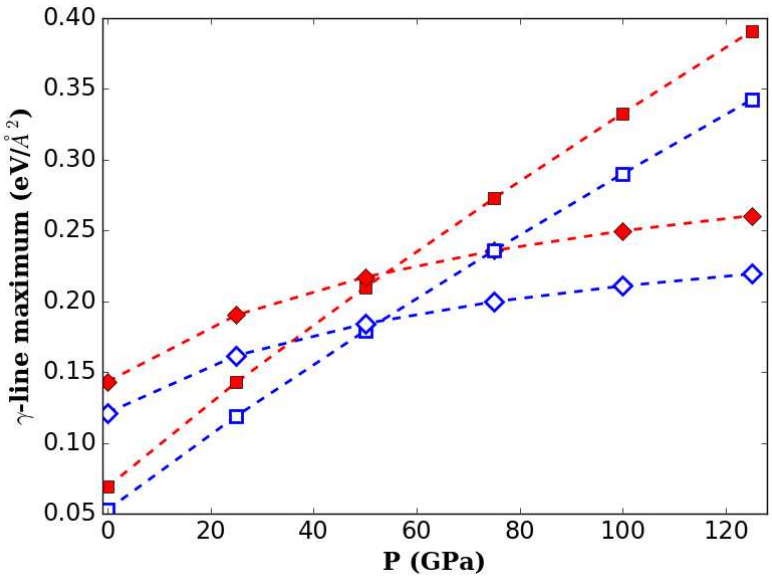

682

683 **Fig. 3** Pressure dependence of the γ-line maximum for slip along 1/2<110> on the {100}
684 (diamonds) and {110} (squares) planes, with dry and wet values plotted with full and empty
685 symbols, respectively. For wet γ-lines, values are shown only for the lowest energy $\{2H_{Mg}\}^X$
686 configuration for each slip plane.

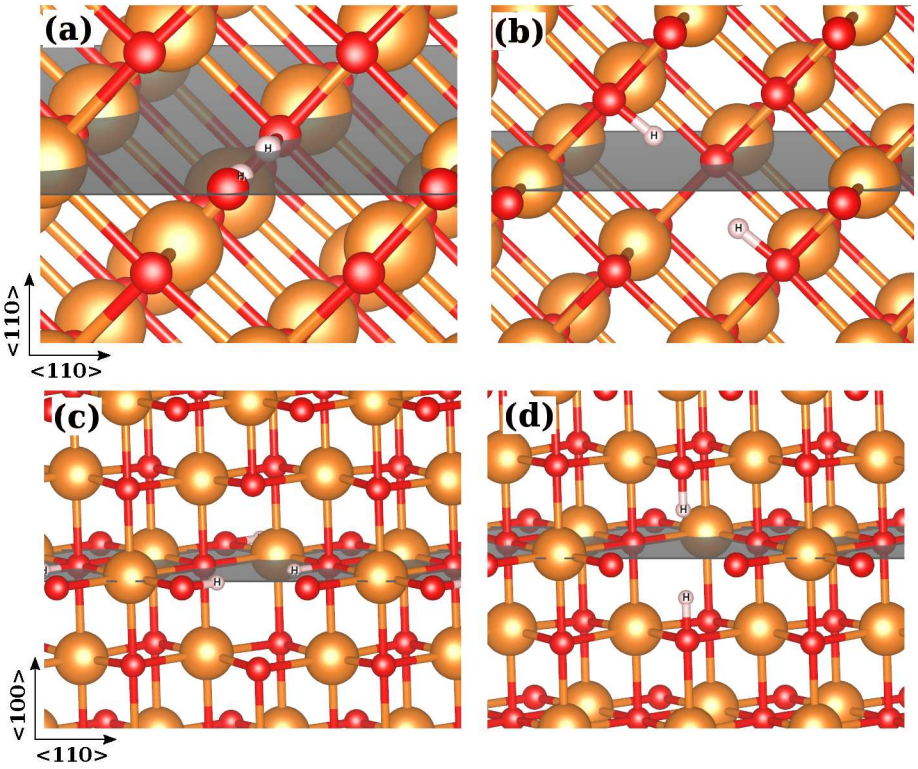

687

688 **Fig. 4** The **s**ymmetrically distinct configurations of the $\{2H_{Mg}\}^X$ defect relative to the {110}
689 stacking fault plane correspond to the cases when the O-H bonds are either (a) in the slip plane and
690 parallel to **b**, or (b) crossing the slip plane. For a $\{2H_{Mg}\}^X$ defect on a {100} stacking fault, the two
691 symmetrically distinct configurations are those with (c) the O-H bond in the slip plane and (d)
692 normal to the slip plane.

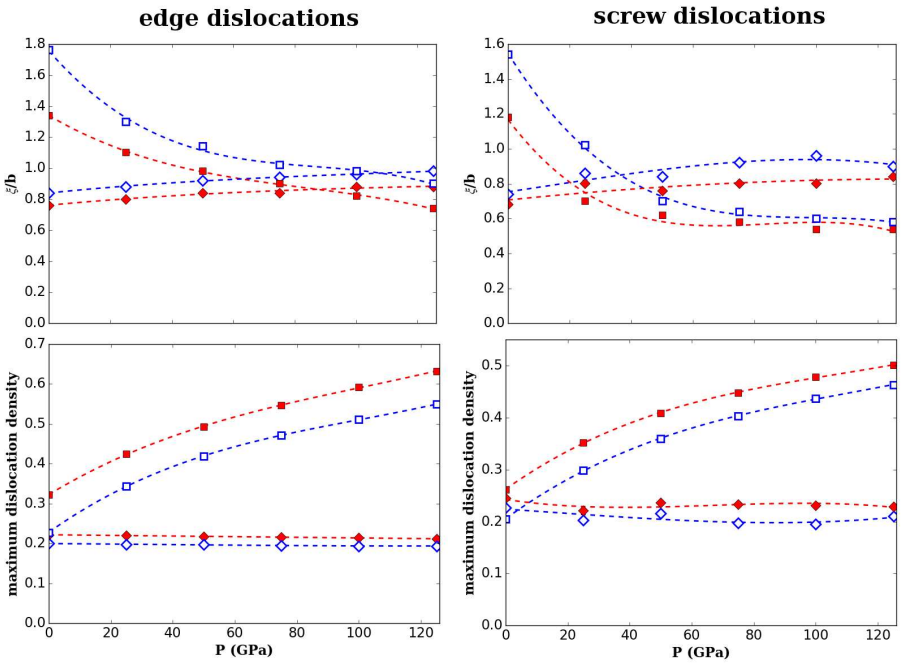

693

694 **Fig. 5** Pressure dependence of the dislocation core width, as a fraction of the Burger's vector
695 magnitude |**b**| (top) and maximum dislocation density along the glide plane (bottom). Results for
696 the 1/2<110>{110} and 1/2<110>{100} slip systems are shown with square and diamond symbols,
697 respectively, while values for hydrous MgO are indicated with hollow symbols.

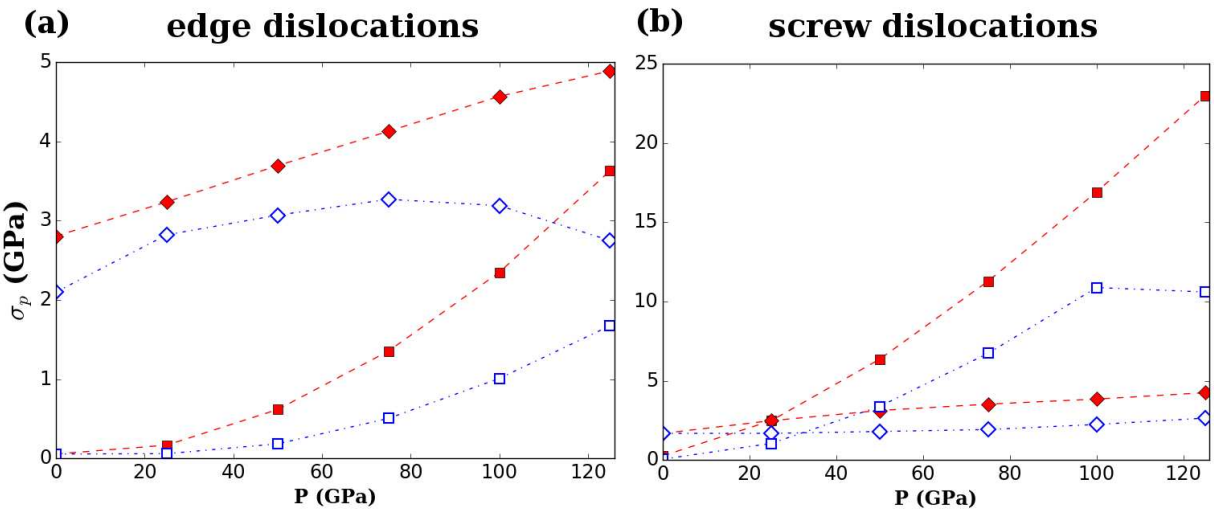

698

Fig. 6 Pressure dependence of the Peierls stresses calculated for (a) glide of edge dislocation, and (b) screw dislocations. Square and diamond symbols correspond to the {110} and {100} glide planes, while filled and hollow symbols are used to represent σ_p in anhydrous and hydrous MgO.

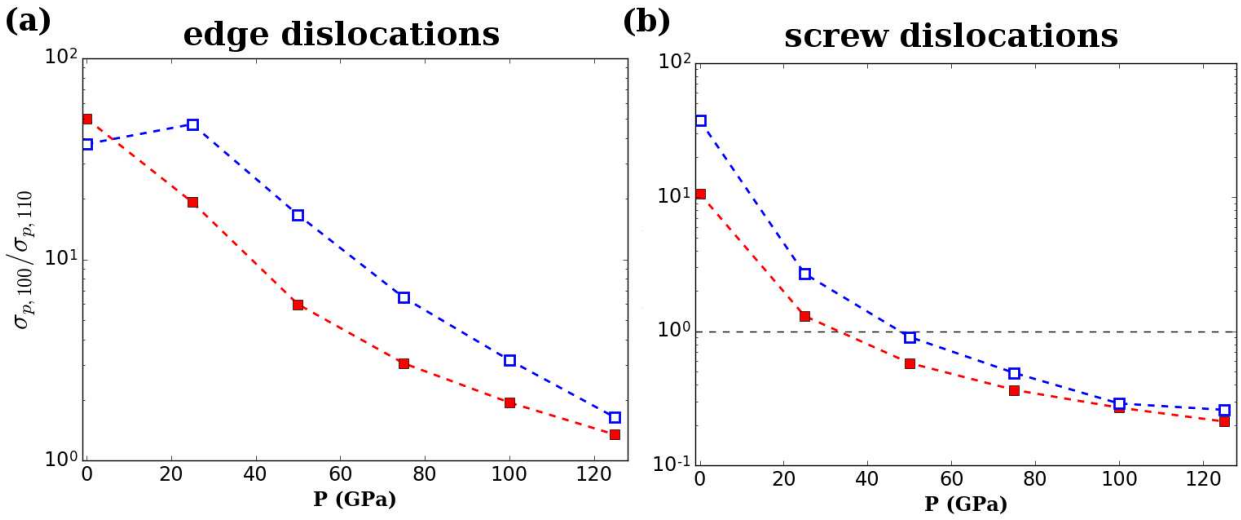

Fig. 7 Ratio of σ_p for glide on {100} and {110} for (a) edge and (b) screw dislocations, with (filled symbols) and without (hollow symbols) $\{2H_{Mg}\}^X$ defects present. The horizontal dashed line for the screw dislocations represents a Peierls stress ratio of 1.